

Rotation symmetry mismatch and interlayer hybridization in MoS₂-black phosphorus van der Waals heterostructures

Received: 23 July 2024

Accepted: 9 January 2025

Published online: 17 January 2025



Zailan Zhang¹, Alberto Zobelli^{2,3}✉, Chaofeng Gao⁴, Yingchun Cheng⁴, Jiuxiang Zhang², Jonathan Caillaux², Lipeng Qiu⁵, Songlin Li⁵, Mattia Cattelan⁶, Viktor Kandyba⁶, Alexei Barinov⁶, Mustapha Zaghioui⁷, Azzedine Bendounan³, Jean-Pascal Rueff³, Weiyan Qi⁸, Luca Perfetti⁸, Evangelos Papalazarou², Marino Marsi²✉ & Zhesheng Chen⁹✉

Interlayer coupling in 2D heterostructures can result in a reduction of the rotation symmetry and the generation of quantum phenomena. Although these effects have been demonstrated in transition metal dichalcogenides (TMDs) with mismatched interfaces, the role of band hybridization remains unclear. In addition, the creation of flat bands at the valence band maximum (VBM) of TMDs is still an open challenge. In this work, we investigate the electronic structure of monolayer MoS₂-black phosphorus heterojunctions with a combined experimental and theoretical approach. The disruption of the rotational symmetry of the MoS₂ bands, the creation of anisotropic minigaps and the appearance of flat bands at the Γ valley, accompanied by the switch of VBM from K to Γ , are clearly observed with micro-ARPES. Unfolded band structures obtained from first principles simulations precisely describe these multiple effects – all independent of the twist angle – and demonstrates that they arise from strong band hybridization between Mo d_{z^2} and P p_x orbitals. The underlying physics revealed by our results paves the way for innovative electronics and optoelectronics based on TMDs superlattices, adding further flexibility to the approaches adopted in twisted hexagonal superlattices.

Vertical structures of layered graphene or transition metal dichalcogenides (TMDs) can be produced very efficiently by simple superposition of individual layers. The twist between the crystals and a possible lattice mismatch leads to 2D moiré superlattices, that may also be accompanied by symmetry breaking and strong bands

hybridization effects. In most studied cases, the individual layers present a three- or six-fold rotational symmetry (C_3 or C_6) which is preserved in the stack. Over the last decade, it has been demonstrated that such systems can exhibit unique physical properties such as unconventional superconductivity, moiré excitons, Wigner crystalline states,

¹School of Physics, Nanjing University of Science and Technology, Nanjing 210094, People's Republic of China. ²Laboratoire de Physique des Solides, CNRS, Université Paris-Saclay, 91405 Orsay, France. ³Société Civile Synchrotron Soleil, L'Orme des Merisiers, Départementale 128, Saint-Aubin 91190, France. ⁴Key Laboratory of Flexible Electronics & Institute of Advanced Materials, Jiangsu National Synergetic Innovation Center for Advanced Materials, Nanjing Tech University, Nanjing 211816, People's Republic of China. ⁵National Laboratory of Solid State Microstructures, and School of Electronic Science and Engineering, Nanjing University, Nanjing 210023, People's Republic of China. ⁶Elettra-Sincrotrone Trieste SCpA, Basovizza, Trieste, Italy. ⁷Laboratoire GREMAN CNRS-UMR 7347 IUT de BLOIS, 41029 Blois, Cedex, France. ⁸Laboratoire des Solides Irradiés, CEA/DRF/IRAMIS, Ecole Polytechnique, CNRS, Institut Polytechnique de Paris, F-91128 Palaiseau, France. ⁹School of Material Science and Engineering, Nanjing University of Science and Technology, Nanjing 210094, People's Republic of China. ✉ e-mail: alberto.zobelli@universite-paris-saclay.fr; marino.marsi@universite-paris-saclay.fr; zhesheng.chen@njtu.edu.cn

and orbital ferromagnetism^{1–12}. In twisted bilayer TMDs, flat bands can be possibly generated for “magic” twisted angles and the Coulomb interaction dominates over kinetic energy due to the small group velocity. However, flat bands have been observed only below the valence band maximum (VBM) at the Γ valley and the generation of these electronic structures at the highest occupied states, where original quantum phenomena are supposed to occur, remains an open challenge^{13–15}.

Stacking layers from different crystal classes also permits breaking the rotational symmetry of the individual layers, giving rise to original functionalities. In such a case, the original C_3 symmetry of the TMDs cannot be preserved anymore^{16–21}. Recent works have demonstrated that the C_3 symmetry breaking induced on TMDs monolayers deposited onto rectangular lattices such as black phosphorus (bP) or silicon phosphide (SiP) leads to the appearance of a spontaneous photocurrent which can even be spin-polarized under circularly polarized light illumination^{17,18}. Although band hybridization between layers has been evoked to possibly trigger this effect, direct experimental evidence of it is still lacking. Furthermore, the physics behind the C_3 symmetry breaking in TMD monolayers remains understudied to date. These questions can be effectively addressed via a direct visualization of the electronic band structure. New developments in micro-angle-resolved photoemission spectroscopy (micro-ARPES) can now provide the necessary space resolution to study these reduced-size heterostructures with the further advantage of providing both a high energy and momentum resolution^{22–29}.

In this work, this technique was used to directly investigate modifications of the electronic structure of monolayer MoS₂ deposited on bP due to the reduction in the rotational symmetry resulting from the combination of crystals belonging to different classes. Irrespective of the twist angles, we observe a breaking of the C_3 symmetry for the highest occupied MoS₂ states and the opening of minigaps at the Γ valley, the properties of which depend on the orientation of the underlying bP layer. In addition, the top valence band at Γ is flat along most of the in-plane directions and undergoes a giant energy renormalization of -140 meV leading to a switch of the VBM from the K point to the Γ point. All these effects are accounted for by first-principle simulations, indicating they derive from a strong hybridization between the Mo d_{z^2} orbitals of the monolayer and P p_x orbitals of the substrate. This understanding of the electronic structure modulation in monolayer MoS₂ induced by the substrate bP involving rotational symmetry breaking and interlayer hybridization opens up possibilities for generating flat bands with arbitrary twist angles in 2D heterostructures and manipulating anisotropic properties in TMDs.

Results

C_3 rotational symmetry breaking and minigap opening

Two MoS₂-bP stacks with different twist angles have been fabricated in a glove box by the dry transfer method (see the “Methods” section). A hexagonal boron nitride (BN) flake (thickness ~10 nm) has been used as a substrate, being free of dangling bonds and charge traps. A multilayer crystal of bP (thickness ~20 nm) was then deposited on it, followed by a monolayer of MoS₂ (a micrograph of the stack can be seen in Supplementary Fig. 1). The twist angle θ between the layers is defined as the angle between the bP and MoS₂ armchair directions (AC) or equivalently in the momentum space as the angle between the bP Γ - X direction and the MoS₂ Γ - M direction (anti-clockwise angles are defined as positive), as shown in Fig. 1a. In Fig. 1b, c is given as example the direct and the reciprocal space of a stack with a twist angle of $\theta = 45^\circ$, as well as the superlattice obtained from the lattice coincidence method imposing a reduced strain on the primitive's lattice parameters.

Figure 1d depicts the configuration of micro-ARPES measurements on MoS₂-bP superlattices. Micro-ARPES experiments were carried out at the Spectromicroscopy beamline of the Elettra synchrotron

light source using photons with energies of $h\nu = 27$ eV and $h\nu = 74$ eV (see the “Methods” section). A scanning photoemission microscopy image (SPEM) of the first MoS₂-bP stack is shown in Fig. 1e (see Supplementary Fig. 2 for the optical images and the second stack). One can clearly distinguish the MoS₂ and MoS₂-bP regions by comparing the total photoelectron intensity in the SPEM with the optical image. The high quality of the MoS₂ monolayer both in the BN and bP regions is confirmed by Raman spectra obtained after performing the micro-ARPES experiments (see Supplementary Fig. 3). The AC direction of the bP crystal can be determined by analyzing the angular dependence of the A_g^2 peak intensity in angle-resolved polarized Raman spectra (ARPRS, see the “Methods” section), as shown in Fig. 1f. The monolayer MoS₂ Γ - K and Γ - M directions can be extracted instead from micro-ARPES constant energy cuts at $E = E_{\text{VBM}}$ (kinetic energy at valence band maximum) and $E = E_{\text{VBM}} - 0.8$ eV. As a result, a twist angle of $\theta = 8.5^\circ \pm 0.5^\circ$ is determined for the first MoS₂-bP stack and $\theta = 2.4^\circ \pm 0.5^\circ$ for the second one (see Supplementary Fig. 4 for $\theta = 2.4^\circ$).

In Fig. 2a–c are presented constant-energy cuts of the 3D micro-ARPES intensity maps taken under $h\nu = 74$ eV obtained for the pristine monolayer and the two MoS₂-bP heterostructures (the Brillouin zone BZ of each material and their relative orientation are depicted in the left panels). The kinetic energy of the top Γ valley ($E_{\text{VBM}\Gamma}$) has been used as an energy reference. For pristine MoS₂, a near-circular shape is observed around Γ for energies close to the $E_{\text{VBM}\Gamma}$ (Fig. 2a) while at lower energies a hexagonal shape appears at higher momenta (see Supplementary Fig. 5). These findings confirm the isotropy of the MoS₂ Γ valley and the overall reciprocal space C_3 symmetry, taking into account the inequivalence between the K and K' valleys due to spin-orbit coupling.

C_3 symmetry breaking in monolayer MoS₂ can introduce Berry curvature dipole and valley magneto-electricity^{30,31}. For both MoS₂-bP heterostructures, the C_3 symmetry is instead broken, as it can be clearly observed in Fig. 2b, c. Constant-energy cuts at $E - E_{\text{VBM}\Gamma} = 0$ meV and $E - E_{\text{VBM}\Gamma} = -100$ meV present a significant deformation along the high symmetry directions of the bP crystal, indicating an effective coupling of the MoS₂ monolayer with the bP substrate. Moreover, constant energy cuts at $E - E_{\text{VBM}\Gamma} = -200$ and -300 meV show an uneven spectral weight along the bands. This characteristic is a result of a gap opening, as evident from the band structures presented in Fig. 2d, e. The band structure of pristine monolayer MoS₂ shows a parabolic dispersion at Γ from which a hole effective mass of $m^* = 2.3 \pm 0.1 m_e$ can be extracted by fitting the experimental data. Instead, minigaps are clearly visible in the band structure of MoS₂ obtained from the two stacks. As one moves from the AC to the zigzag (ZZ) bP directions, these minigaps shift to larger wave vectors and decrease in width. Intriguingly, the top valence band at Γ bands undergoes a significant transformation, becoming completely flat as shown for the $AC \pm 45^\circ$ directions. Along the ZZ direction, a small dispersion is preserved, and the extracted holes' effective masses are $m^* = 8.1 \pm 0.1 m_e$ in the $\theta = 8.5^\circ$ sample and $m^* = 3.0 \pm 0.1 m_e$ in the $\theta = 2.4^\circ$ sample. The origins of MoS₂ band modifications and the discrepancy of effective masses along the ZZ direction between the two samples are discussed in the next section.

The observed C_3 symmetry breaking, minigap opening, and band flattening in MoS₂-bP superlattices are also evident at a photon energy of $h\nu = 27$ eV (see Supplementary Figs. 6 and 7). It is worth noting that photoemission signals of bP are too weak to be observed in both samples, even though they have been previously clearly observed in bulk crystals^{32–35}. Two reasons account for the absence of the bP photoemission signal in MoS₂-bP heterostructures. First, the electron mean free path for a kinetic energy of ~ 20 or ~ 70 eV is $\sim 5 \text{ \AA}$ ³⁶, comparable to the thickness of the monolayer MoS₂ ($\sim 6 \text{ \AA}$)³⁷, mainly explaining the absence of signal from bP in the MoS₂-covered regions. Second, ultrafast surface degradation of bP is unavoidable during the

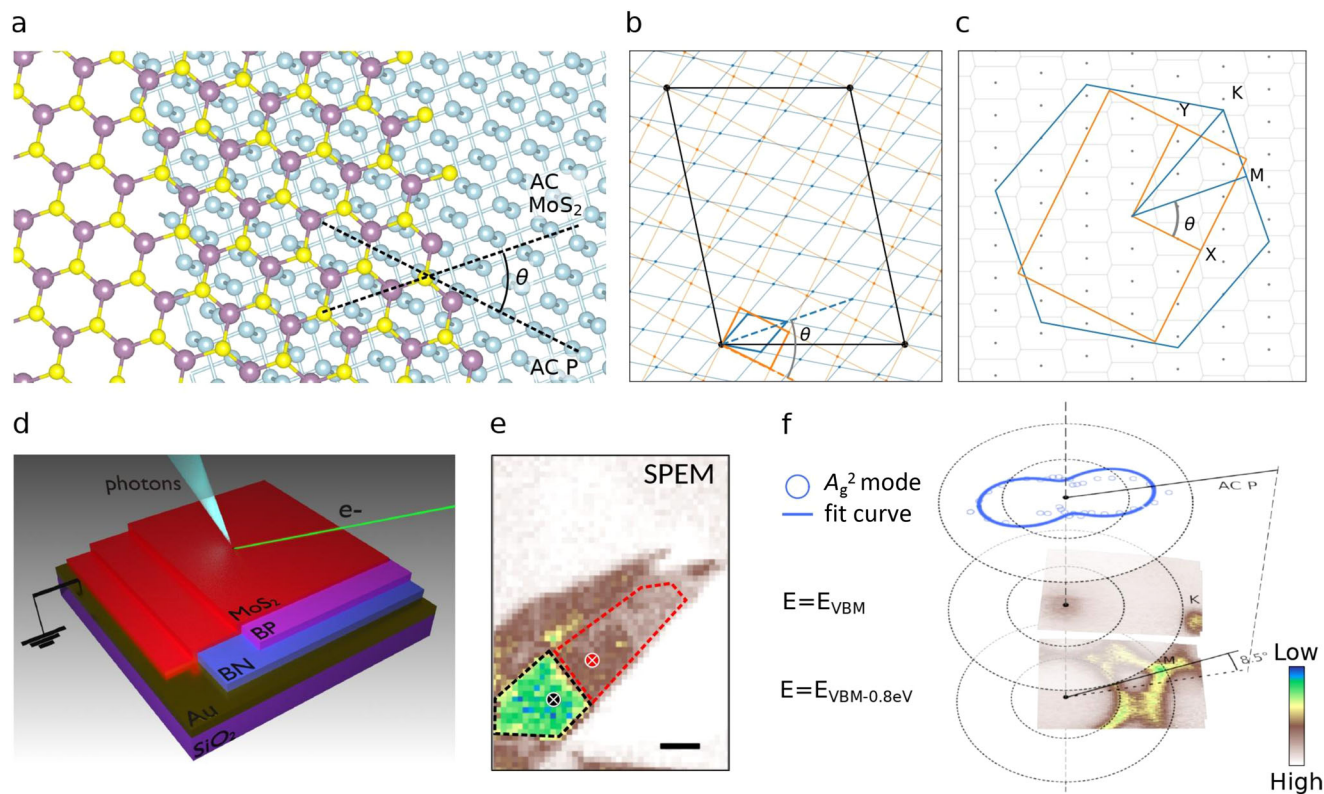


Fig. 1 | Schematics of MoS₂-black phosphorus (MoS₂-bP) superlattice and micro-angle-resolved photoemission spectroscopy (micro-ARPES). **a–c** Schematics of atomic structure and corresponding Brillouin zone (BZ) of MoS₂-bP superlattices, with twisted angle θ . The armchair (AC) directions of MoS₂ and bP are labeled as dashed lines in panel **a**. **d** Schematic of micro-ARPES on MoS₂-bP superlattices. **e** Scanning photoemission microscopy image (SPM) of MoS₂-bP superlattice ($\theta = 8.5^\circ$). The photoemission signals are integrated from the energy range of

binding energy 2.1–2.3 eV and momentum range of $k_{\parallel} = \pm 0.4 \text{ \AA}^{-1}$. Monolayer MoS₂ and MoS₂-bP regions are labeled in black and red dashed curves, and the measured points of micro-ARPES are labeled as circular shapes in the regions. The scale bar is 5 μm . **f** Determination of twisted angle θ . The angle-resolved polarized Raman spectra (ARPRS) of A_g^2 vibration mode in bP with fitted curve (top) and the micro-ARPES of monolayer MoS₂ at constant energy cuts of kinetic energy at valence band maximum $E = E_{\text{VBM}}$ (middle) and $E = E_{\text{VBM}} - 0.8 \text{ eV}$ (bottom).

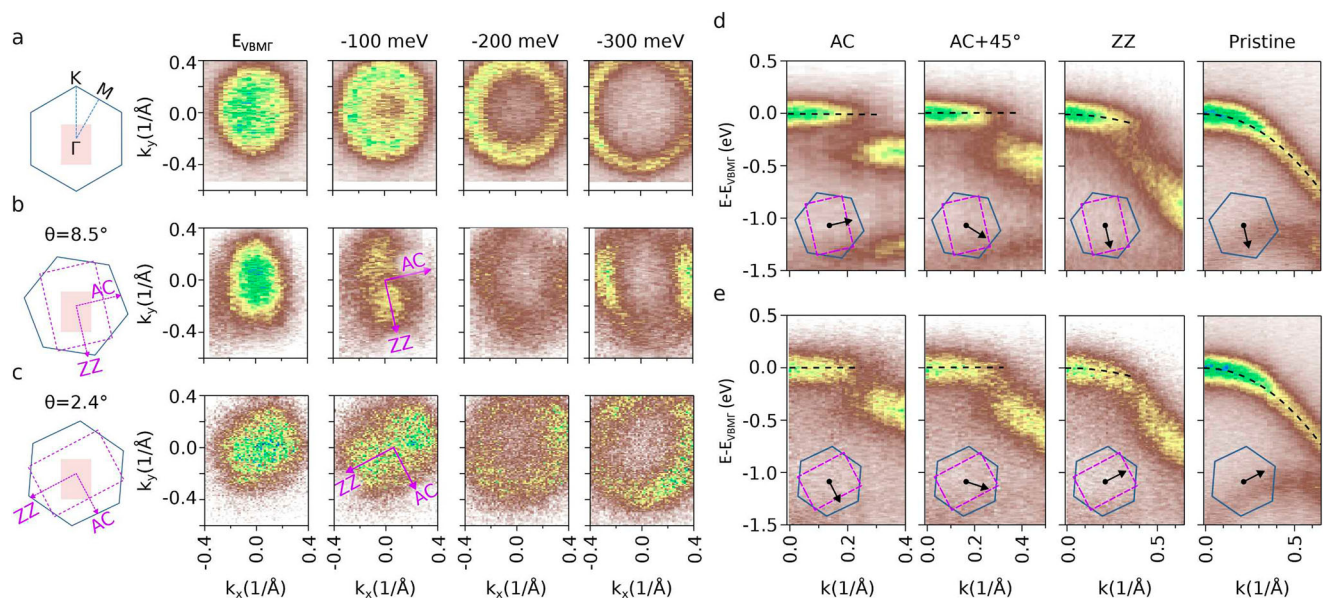


Fig. 2 | Rotation symmetry breaking, minigap opening, and flat bands at Γ valley of MoS₂-bP superlattices. **a–c** Constant energy cut maps of monolayer MoS₂, MoS₂-bP superlattices with $\theta = 8.5^\circ$ and with $\theta = 2.4^\circ$. The corresponding BZ and orientations are depicted in the left panel. **d** and **e** Valence bands of MoS₂-bP

along AC, AC + 45° and zigzag (ZZ) directions in superlattices with $\theta = 8.5^\circ$ (top) and $\theta = 2.4^\circ$ (bottom). The valence bands of monolayer MoS₂ are given for comparison in the right panel. The bands are fitted by dashed curves. The cut directions are labeled in the BZ inserted in each panel.

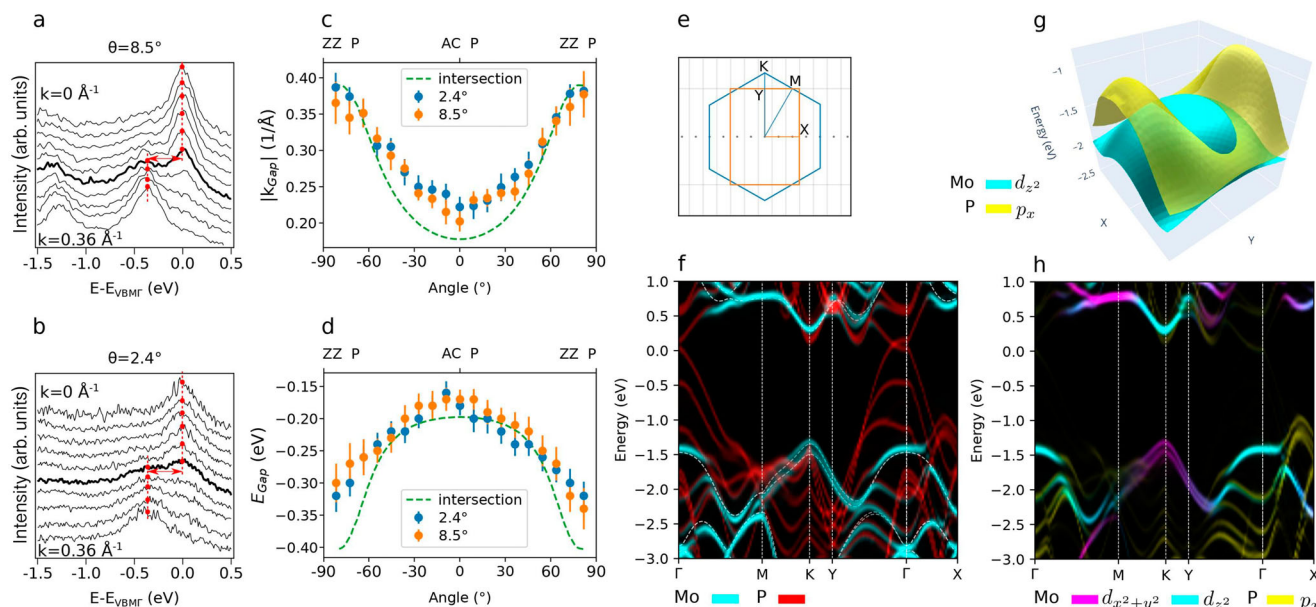


Fig. 3 | Anisotropic properties of minigaps and theory calculation of band hybridization in MoS₂-bP superlattices. **a** and **b** Energy distribution curves (EDCs) extracted from MoS₂-bP superlattices with $\theta = 8.5^\circ$ in **a** and $\theta = 2.4^\circ$ in **b** along AC direction from $k = 0 \text{ \AA}^{-1}$ to $k = 0.36 \text{ \AA}^{-1}$. The red points and red arrows indicate the peak positions and hybridized gap size, respectively. The highlighted black curves represent the approximate momentum position of the gap. **c** and **d** Extracted momentum and energy positions of hybridized minigap from micro-ARPES data and simulated intersection positions from panel **g** as a function of

directions. **e** The reciprocal space of a MoS₂-bP superstructure model with a twist angle of $\theta = 0^\circ$. **f** The corresponding unfolded band structure projected on the MoS₂ (cyan) and bP (red) layers. **g** The Mo d_{z^2} band (cyan) of monolayer MoS₂ around the center of the BZ together with the P p_x band (yellow) of bulk bP. The bands have been aligned accordingly to density functional theory (DFT) simulations of the heterostructure. **h** The unfolded bands projected onto Mo d_{z^2} (cyan) and $d_{x^2-y^2}$ (magenta) and P p_x orbitals (yellow).

fabrication process³⁸ although this is difficult to quantify. Despite this, it is important to note that the samples are never exposed to the ambient conditions prior to the micro-ARPES measurements, which preserves most of the bP quality, as evidenced by the sharp Raman signal. Moreover, the significant band renormalization observed in the MoS₂/bP heterostructure aligns well with our theoretical calculations presented in the following section, suggesting that bP plays a dominant role in the interface coupling even though the photoemission signal of bP is not evident.

Anisotropic properties of the minigaps and orbital hybridization

In order to further investigate the anisotropic properties of the minigaps, we extract their size, momentum, and energy position by analyzing micro-ARPES energy distribution curves (EDCs) obtained along different directions of the bP crystal; as an example in Fig. 3a, b are presented EDCs along the AC direction for the two stacks. The minigap width can be estimated from the energy distance between contiguous peaks, as indicated by the double arrow in the figure. In Fig. 3c, the results for the gap momentum position (k_{Gap} , obtained using the VBM as reference) as a function of the direction angle, and in Fig. 3d for the energy position (E_{Gap} , obtained using the Γ point as reference) are summarized. Both k_{Gap} and E_{Gap} are determined from EDCs as a function of the k -vector, as the minigap appears at positions where the peak shows an abrupt change, as illustrated in Fig. 3a, b. Both curves present a strong anisotropy which follows the bP symmetry. Furthermore, the EDCs reveal that in the broad direction domain of $\text{AC} \pm 60^\circ$, the higher energy peak presents a rather constant energy (see for instance, Fig. 3a, b for the AC direction). This observation indicates a flattening of the top valence band at Γ , to which is associated with a significant increase in the density of states (DOS). The same angular dependence is found for the two stacks indicating that the MoS₂-bP twist angle is not critical for the generation of minigaps and flat bands. This result is in strong contrast with the case of twisted TMDs bilayers,

where flat bands occur only at discrete twist “magic” angles. Indeed, flat minibands in twisted bilayer WSe₂ were experimentally observed via micro-ARPES in the Γ valley only at twist angles of 5.1° , 5.3° , and 57.4° ; no flat minibands were detected in the K valleys, likely due to a reduced interlayer wavefunction overlap^{13–15}.

To gain more insight into the electronic structure at the Γ valley of MoS₂, we performed complementary first-principles simulations of MoS₂-bP superstructure models. The band structure of a moiré supercell heterostructure is highly folded, making it challenging to correlate with the individual components. This complexity can be addressed through the use of unfolding methods, which offer a primitive cell-effective band structure that can be compared with ARPES measurements. For heterostructures formed from layers with incommensurate lattice parameters, a supercell can be built using the lattice coincidence method. This method identifies pairs of supercells that can be combined to minimize lattice mismatch, allowing the residual strain to be distributed across one or both layers. The coincidence method is commonly used for 2D heterostructures formed by stacking two hexagonal lattices, such as graphene and h-BN, resulting in a hexagonal supercell. In our work, we extend this approach to heterostructures involving both rectangular and hexagonal lattices. For these general heterostructure models, oblique supercells are obtained, requiring both lattice parameters and angles to align, which significantly reduces the number of feasible supercells for a given strain tolerance (see Supplementary Fig. 8). Figure 3e shows the reciprocal space of a MoS₂-bP superstructure model with a twist angle of $\theta = 0^\circ$ and Fig. 3f the corresponding unfolded band structure projected on the MoS₂ (cyan) and bP (red) layer. The band structure of pristine MoS₂ is overlaid as a dashed curve for comparison. The simulation clearly reproduces the minigaps and band flattening in MoS₂-bP superlattices observed by micro-ARPES. We further calculated the unfolded bands over a homogeneous mesh of the reciprocal space; an excellent agreement is also observed between the unfolded bands and micro-ARPES when comparing the intensity distribution at equivalent energy

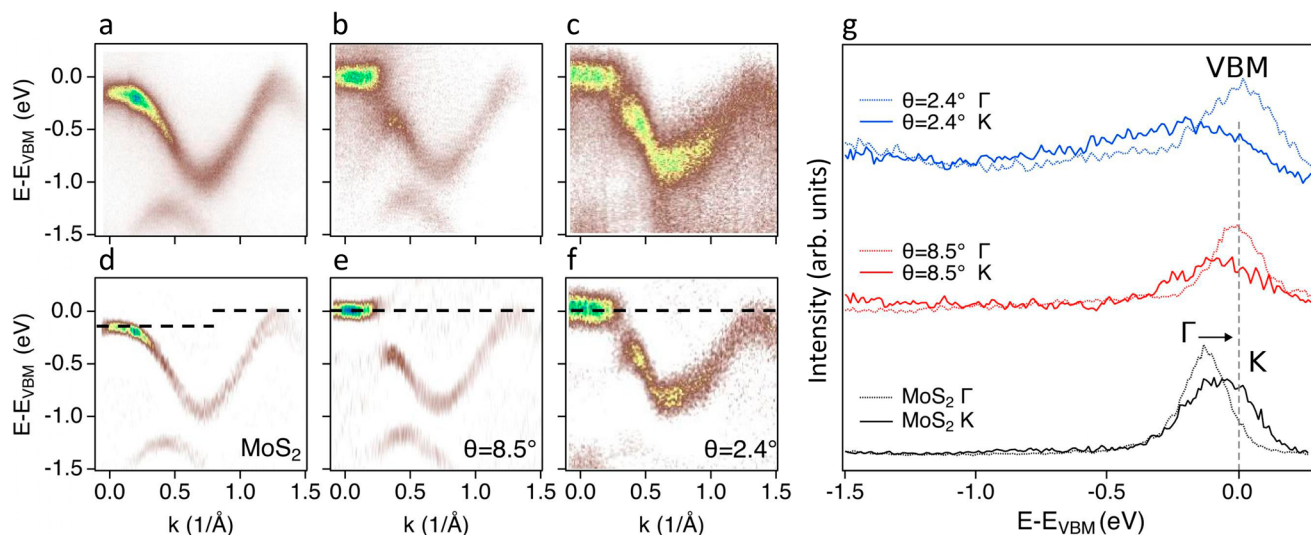


Fig. 4 | Flat band in VBM of MoS₂. **a–c** Micro-ARPES from pristine monolayer MoS₂ (left) and MoS₂-bP superlattices with $\theta = 8.5^\circ$ (middle) and $\theta = 2.4^\circ$ (right) along the Γ - K direction closest to AC direction. **d–f** The corresponding second derivatives of

panels **a–c**. The dashed lines represent the highest energy levels at the Γ and K points. **g** EDCs of pristine monolayer MoS₂ and MoS₂-bP superlattices taken at momentum positions of Γ and K points. The VBM is indicated by the line.

cuts (see Supplementary Fig. 9). Remarkably, a strong hybridized feature and additional bands along a direction parallel to Γ - Y at $k_x = 0.2 \text{ \AA}^{-1}$ are formed which we ascribe to hybridized bands and possible moiré effect in the superlattice (see Supplementary Fig. 10).

Figure 3h presents the unfolded bands projected onto $\text{Mo}d_{z^2}$ (cyan) and $d_{x^2+y^2}$ (magenta) and $\text{P}p_x$ (yellow) orbitals, demonstrating that minigaps occur due to avoid band crossing, indicating a rehybridization of MoS₂ d_{z^2} and bP p_x surface orbitals; orbitals with other symmetries (see Supplementary Fig. 11) do not hybridize between the layers. Mo and P atoms are not aligned directly on top of one another, which suggests that hybridization between out-of-plane orbitals may be less significant than expected. Instead, this spatial arrangement allows for an overlap between Mo $d_{x^2+y^2}$ and P in-plane orbitals, which is less sensitive to the exact relative positions of atoms between the layers. Additionally, an energy and momentum match is achieved between bands with Mo d_{z^2} and $\text{P}p_x$ characters, while these conditions are not satisfied for $\text{P}p_y$ orbitals, which lie at a lower energy level. This result is also confirmed by the simulation of a heterostructure model with a larger twist angle $\theta = 22^\circ$ (see Supplementary Fig. 12).

Figure 3g presents the $\text{Mo}d_{z^2}$ band of the perfect monolayer MoS₂ around the center of the BZ together with the p_x band of bulk bP; the bands have been aligned accordingly to DFT simulations of the heterostructure. The two surfaces cross in space over a line whose energy and momentum angular dependence, indicated by dashed lines in Fig. 3c, d, follows the positions of the minigaps observed in the experiments. Since the Mo d_{z^2} band is essentially isotropic at the Γ valley, the rotation of the bP layer does not change the shape of the crossing curve but its orientation. As a result, the properties of such band modifications at the Γ valley of MoS₂ are determined solely by the in-plane of bP. This simple model explains why the C_3 symmetry breaking, the appearance of minigaps, and the flat band at the Γ valence valley are independent of the twist angle between MoS₂ and bP. It is important to note that the Mo d_{z^2} and $\text{P}p_x$ band alignment, determined by the work functions and doping levels of MoS₂ and bP, plays a critical role in band tuning. This alignment is especially crucial in determining the effective masses of MoS₂ bands along the ZZ direction, where the Mo d_{z^2} and $\text{P}p_x$ bands do not present real intersections. As an example, let us consider the two samples shown in Fig. 2d and e: the effective masses of MoS₂ bands along the ZZ direction present clearly different values, and we attribute this to slight

differences in band alignment between MoS₂ and bP, rather than the twist angle. First, the monolayer MoS₂ is likely extrinsically doped during the fabrication process, resulting in minor differences in the doping levels of pristine MoS₂ between the two samples. Additionally, the thickness of bP in the two samples is not the same, as indicated by the optical contrast, which can also contribute to variations in the $\text{P}p_x$ band. Overall, the band alignment between MoS₂ and bP dominates the results of band hybridization in the MoS₂-bP heterostructure.

Flat band in the VBM of monolayer MoS₂

Another important effect of the interactions with the bP substrate is the displacement of the valence band maximum in the momentum space. Figure 4a–f shows the valence bands and their second derivative along the Γ - K direction in pristine monolayer MoS₂ and in the two MoS₂-bP heterostructures with different twist angles. The spin-orbit coupling (SOC) splitting at the K point in pristine monolayer MoS₂ is observed from the second derivative data shown in Fig. 4d, while it is difficult to discern in the MoS₂-bP heterostructure regions, mainly due to band broadening, as the roughness of the bP is greater than that of BN. Independently in all the presented graphs, the energy at VBM has been chosen as reference energy. As expected, in monolayer MoS₂ the VBM at K is about 120 meV higher than at Γ , which shows a similar character to the previous reports^{39–41}. However, in the MoS₂-bP heterostructures, the relative energy positions between Γ and K are inverted, and the VBM occurs at Γ , where the flat band is located, as indicated by the black dashed lines in Fig. 4d–f. The corresponding EDCs obtained at the Γ and K points also clearly demonstrate the VBM renormalization, as presented in Fig. 4g. Once more the magnitude of this effect is the same for the two twist angles. Such flat bands at the VBM can potentially improve the transport properties or thermoelectric properties, such as the Seebeck coefficient in MoS₂⁴⁰.

This band normalization can also be observed on the calculated band structure (Fig. 3h) or on the projected density of states (see Supplementary Fig. 13). Monolayer MoS₂ is a direct bandgap semiconductor with a gap at K where the highest occupied state has a $d_{x^2+y^2}$ character and the lowest unoccupied a d_{z^2} character³⁴; the top valence band at Γ is also built from d_{z^2} orbitals. The same characters are preserved in the heterostructure (Fig. 3h), but the relative position of the states is significantly modified. The valence band maximum moves to Γ while both extrema in the K valley remain unchanged.

Discussion

In summary, we have directly investigated the electronic band structure renormalization in monolayer MoS₂ at rotational symmetry mismatched interface MoS₂-bP by using micro-ARPES and first principle simulations. As a result of a strong band hybridization between the Mo and P orbitals in the heterojunction, the electronic structure of MoS₂ gets strongly modified with a breakdown of the C₃ symmetry, the opening of anisotropic minigaps, and a flattening of the upper valence band, all irrespective of the twist angle. Moreover, a band renormalization of the order of ~140 meV is realized, which results in a transition of the VBM from *K* to the flat band occurring at the *Γ* valley. Our results clearly identify the underlying physics which is at the origin of all these effects—namely the combined effects of band hybridization and strong interlayer coupling with rotational symmetry mismatch at the heterojunction. As a result, our discoveries pave the way for extrapolating these findings to diverse heterostructures, offering a novel avenue to manipulate rotational symmetry and valley renormalization in TMDs, without relying on external pressure or conventional methods of controlling twisted angles. More generally, the flat band generated at the VBM of TMDs offers a highly tunable platform for studying strongly correlated physics, given the large effective masses and relatively strong electron–electron interactions that TMDs exhibit. Notably, previous transport studies have shown that the Fermi level can reach the flat band through effective gating in TMD devices. In the rotation symmetry mismatched MoS₂-bP interface we proposed, the anisotropic band flattening at the VBM of MoS₂ expands the platform for exploring anisotropic strongly correlated physics in monolayer TMDs. Moreover, the C₃ rotational symmetry breaking, which originates from band hybridization, offers the potential for non-linear physics applications, such as the generation of shift current in TMDs-bP-based photovoltaic devices. Overall, our results reveal a wide range of possibilities to discover in TMDs anisotropic behaviors and exotic physical phenomena, such as the appearance of strongly correlated phases associated with flat bands.

Methods

Sample preparation

In the sample fabrication process, we used the dry transfer method to fabricate MoS₂-bP superlattices in the glove box. Firstly, multilayer BN, multilayer bP, and monolayer MoS₂ were exfoliated onto different silicon oxide–silicon (SiO₂-Si) substrates, respectively. The MoS₂-bP vertical structures were fabricated by stacking flakes together with high precision under optical microscopy. Firstly, monolayer MoS₂ was transferred onto a polycarbonate (PC) film on polydimethylsiloxane (PDMS) stamp. Secondly, the bP flake was well aligned by PDMS-PC-MoS₂ and then peeled off from SiO₂-Si substrate, forming PDMS-PC-MoS₂-bP structure. Thirdly, the BN flake was continually transferred onto PDMS-PC-MoS₂-bP and thus giving PDMS-PC-MoS₂-bP-BN structure by using a similar way. The PDMS-PC-MoS₂-bP-BN was placed on Au/SiO₂/Si substrate, and then the PDMS stamp was smoothly peeled off from PC-MoS₂-bP-hBN after heating it at -120 °C. At last, the PC film was removed by washing the PC-MoS₂-bP-BN in chloroform solvent, followed by drying in the glove box.

Micro-ARPES experiments

Micro-ARPES measurements of MoS₂-bP superlattices were performed at the spectromicroscopy beamline of the Elettra light source in Italy. In order to clean the sample surface, the samples were annealed at -200 °C for 3 h in the preparation chamber under ultrahigh vacuum before micro-ARPES experiments. The pressure in the experimental chamber was better than 1×10^{-10} mbar during micro-ARPES measurements. At Spectromicroscopy beamline, linearly *p*-polarized light with a fixed incident angle of 45° was focused to ~600 nm by Schwartzschild objective. Momentum space mapping was carried out by the rotation of a hemispherical analyzer. All the experiments were performed at

$T = -95$ K with photon energy of $h\nu = 27$ eV and $h\nu = 74$ eV. The overall energy and momentum resolution of the experiment was ~45 meV and 0.005 \AA^{-1} .

ARPES experiments

ARPES experiments on MoS₂-bP superlattices with $\theta = 8.5^\circ$ and $\theta = 2.4^\circ$ were performed on Renishaw and Horiba Raman spectrometers, respectively. A continuous Argon laser with a wavelength of 514 nm (Renishaw) and 532 nm (Horiba) through $\times 100$ objective lens was used to excite the sample. The incident light passing through a linear polarizer was reflected by a beam splitter. A half-wave plate was positioned between the beam splitter and the objective lens in order to rotate the polarization of the incident light. Another half-wave plate was positioned in the collection path, followed by a linear polarizer to select the polarization of interest from the scattered light, which was subsequently detected by a CCD camera. The samples were rotated at a step of 10° in order to explore Raman anisotropy of black phosphorus, and the MoS₂-bP area was chosen for the measurement.

Computational details

DFT calculations have been performed using the OpenMX code⁴². The exchange–correlation potential was expressed in the generalized gradient approximation using the Perdew–Burke–Ernzerhof (PBE) schema. Norm conserving full relativistic pseudopotentials, including a partial core correction and spin–orbit coupling, was used. Dispersion interactions have been included using the Grimme-D2 method⁴³. A basis set of optimized numerical pseudo-atomic orbitals was employed as provided by the OpenMX 2019 database. Band unfolding has been performed over a homogeneous mesh of the reciprocal space according to the method presented in refs. 44,45. An energy broadening of 50 meV has been employed to produce all band unfolding figures.

For the structure model: MoS₂ and bP have incommensurable lattice parameters and therefore a moiré supercell cannot be constructed from a simple superposition of the layers but small lattice deformations must be imposed. For band structure calculation with twist angle $\theta = 0^\circ$, a minimal moiré supercell model for the bP-MoS₂ heterostructure on which the AC MoS₂ and BP directions are aligned can be built from supercells obtained from the transformation matrix $\begin{pmatrix} 5 & 0 \\ 0 & 1 \end{pmatrix}_{\text{bP}}$ and $\begin{pmatrix} 4 & -4 \\ 1 & 1 \end{pmatrix}_{\text{MoS}_2}$. To minimize spurious effects on the MoS₂ electronic structure, a moiré supercell has been built by imposing all lattice deformations only to the bP slab (a stretch of about 0.4% along *a* and a strain of about 3.8% along *b*). A slab of six phosphorous atomic planes provides an accurate representation of the bP electronic structure.

Data availability

The main data supporting the findings of this study are available within the article and its Supplementary Information files. All the raw data generated in this study are available from the corresponding author upon request.

Code availability

All the data analysis codes related to this study are available from the corresponding author upon request.

References

1. Foutty, B. A. et al. Mapping twist-tuned multiband topology in bilayer WSe₂. *Science* **384**, 343–347 (2024).
2. Sha, Y. J. et al. Observation of a Chern insulator in crystalline ABCA-tetralayer graphene with spin–orbit coupling. *Science* **384**, 414–419 (2024).

3. Xu, Y. et al. Correlated insulating states at fractional fillings of moiré superlattices. *Nature* **587**, 214–218 (2020).
4. Regan, E. C. et al. Mott and generalized Wigner crystal states in WSe₂/WS₂ moiré superlattices. *Nature* **579**, 359–363 (2020).
5. Wang, L. et al. Correlated electronic phases in twisted bilayer transition metal dichalcogenides. *Nat. Mater.* **19**, 861–866 (2020).
6. Li, T. et al. Continuous Mott transition in semiconductor moiré superlattices. *Nature* **597**, 350–354 (2021).
7. Lu, X. et al. Superconductors, orbital magnets and correlated states in magic-angle bilayer graphene. *Nature* **574**, 653–657 (2019).
8. Serlin, M. et al. Intrinsic quantized anomalous Hall effect in a moiré heterostructure. *Science* **367**, 900–903 (2020).
9. Tschirhart, C. L. et al. Imaging orbital ferromagnetism in a moiré Chern insulator. *Science* **372**, 1323–1327 (2021).
10. Geisenhof, F. R. et al. Quantum anomalous Hall octet driven by orbital magnetism in bilayer graphene. *Nature* **598**, 53–58 (2021).
11. Graham, A. J. et al. Conduction band replicas in a moiré semiconductor heterobilayer. *Nano Lett.* **24**, 5117–5124 (2024).
12. Sinha, S. et al. Berry curvature dipole senses topological transition in a moiré superlattice. *Nat. Phys.* **18**, 765–770 (2022).
13. Gatti, G. et al. Flat moiré bands in twisted bilayer WSe₂. *Phys. Rev. Lett.* **131**, 046401 (2023).
14. Pei, D. et al. Observation of Γ -valley moiré bands and emergent hexagonal lattice in twisted transition metal dichalcogenides. *Phys. Rev. X* **12**, 021065 (2022).
15. Pei, D. et al. Twisted-induced modification in the electronic structure of bilayer WSe₂. *Nano Lett.* **23**, 7008–7013 (2023).
16. Liu, Y. et al. Tailoring sample-wide pseudo-magnetic fields on a graphene-black phosphorus heterostructure. *Nat. Nanotechnol.* **13**, 828–834 (2018).
17. Duan, S. et al. Berry curvature dipole generation and helicity-to-spin conversion at symmetry-mismatched heterointerfaces. *Nat. Nanotechnol.* **18**, 867–874 (2023).
18. Akamatsu, T. et al. A van der Waals interface that creates in-plane polarization and a spontaneous photovoltaic effect. *Science* **372**, 68–72 (2021).
19. Zheng, X. et al. Symmetry engineering induced in-plane polarization in MoS₂ through van der Waals interlayer coupling. *Adv. Funct. Mater.* **32**, 2202658 (2022).
20. Li, Z. et al. An anisotropic van der Waals dielectric for symmetry engineering in functionalized heterointerfaces. *Nat. Commun.* **14**, 5568 (2023).
21. Wu, B. et al. Engineering anisotropy in 2D transition metal dichalcogenides via heterostructures. *Opt. Lett.* **48**, 5876–5870 (2023).
22. Nguyen, P. V. et al. Visualizing electrostatic gating effects in two-dimensional heterostructures. *Nature* **572**, 220–223 (2019).
23. Jones, A. J. H. et al. Observation of electrically tunable van Hove singularities in twisted bilayer graphene from nanoARPES. *Adv. Mater.* **32**, 2001656 (2020).
24. Li, Q. et al. Evolution of the flat band and the role of lattice relaxations in twisted bilayer graphene. *Nat. Mater.* **23**, 1070–1076 (2024).
25. Ulstrup, S. et al. Direct observation of minibands in a twisted graphene/WS₂ bilayer. *Sci. Adv.* **6**, eaay6104 (2020).
26. Katoch, J. et al. Giant spin-splitting and gap renormalization driven by trions in single-layer WS₂/h-BN heterostructures. *Nat. Phys.* **14**, 355–359 (2018).
27. Lisi, S. et al. Observation of flat bands in twisted bilayer graphene. *Nat. Phys.* **17**, 189–193 (2021).
28. Utama, M. I. B. et al. Visualization of the flat electronic band in twisted bilayer graphene near the magic angle twist. *Nat. Phys.* **17**, 184–188 (2021).
29. Ulstrup, S. et al. Observation of interlayer plasmon polaron in graphene/WS₂ heterostructures. *Nat. Commun.* **15**, 3845 (2024).
30. Son, J. et al. Strain engineering of the Berry curvature dipole and valley magnetization in monolayer MoS₂. *Phys. Rev. Lett.* **123**, 036806 (2010).
31. Lee, J. et al. Valley magnetoelectricity in single-layer MoS₂. *Nat. Mater.* **16**, 887–891 (2017).
32. Chen, Z. et al. Band gap renormalization, carrier multiplication, and Stark broadening in photoexcited black phosphorus. *Nano Lett.* **19**, 488–493 (2019).
33. Chen, Z. et al. Spectroscopy of buried states in black phosphorus with surface doping. *2D Mater.* **7**, 035027 (2020).
34. Han, C. Q. et al. Electronic structure of black phosphorus studied by angle-resolved photoemission spectroscopy. *Phys. Rev. B* **90**, 085101 (2014).
35. Kim, J. et al. Observation of tunable band gap and anisotropic Dirac semimetal state in black phosphorus. *Science* **349**, 723–726 (2015).
36. Seah, M. P. et al. Quantitative electron spectroscopy of surface: a standard data base for electron inelastic mean free paths in solids. *Surf. Interface Anal.* **1**, 2–11 (1979).
37. Andrea, S. et al. Emerging photoluminescence in monolayer MoS₂. *Nano Lett.* **10**, 1271–1275 (2010).
38. Abellán, G. et al. Fundamental insights into the degradation and stabilization of thin layer black phosphorus. *J. Am. Chem. Soc.* **139**, 10432–10440 (2017).
39. Jin, W. et al. Direct measurement of the thickness-dependent electronic band structure of MoS₂ using angle-resolved photoemission spectroscopy. *Phys. Rev. Lett.* **111**, 106801 (2013).
40. Hippalgaonkar, K. et al. High thermoelectric power factor in two-dimensional crystals of MoS₂. *Phys. Rev. B* **95**, 115407 (2017).
41. Mak, K. F. et al. Atomically thin MoS₂: a new direct-gap semiconductor. *Phys. Rev. Lett.* **105**, 136805 (2010).
42. Ozaki, T. Variationally optimized atomic orbitals for large-scale electronic structures. *Phys. Rev. B* **67**, 155108 (2003).
43. Grimme, S. Semiempirical GGA-type density functional constructed with a long-range dispersion correction. *J. Comput. Chem.* **27**, 1787–1799 (2006).
44. Ku, W., Berlijn, T. & Lee, C. C. Unfolding first-principles band structures. *Phys. Rev. Lett.* **104**, 216401 (2010).
45. Lee, C. C., Yamada-Takamura, Y. & Ozaki, T. Unfolding method for first-principles LCAO electronic structure calculations. *J. Phys. Condens. Matter.* **24**, 345501 (2013).

Acknowledgements

M.M. acknowledges financial support from “Investissement d’Avenir” Labex PALM (ANR-10-LABX-0039-PALM), and Z.C. acknowledges financial support from Nanjing University of Science and Technology (AE899991/406, and AD411203). Z.C. thanks Elettra Light Source for the provision of micro-ARPES beamtime and European financial support under proposals of Nos. 20205459, 20210106, and 20225263.

Author contributions

Z.Z., A.Z., M.M. and Z.C. conceived and planned the project. C.G. and Y.C. made the sample of $\theta = 8.5^\circ$. Z.Z., L.Q. and S.L. made the sample of $\theta = 2.4^\circ$. A.Z. performed all the theory calculations. Z.C. performed micro-ARPES experiments at the Elettra light source. J.Z., J.C., A.B. and M.Z. contributed to Raman’s characterization. M.C., V.K. and A.B. were responsible for the Spectromicroscopy beamline at Elettra light source. A.B., J.-P.R., W.Q., E.P. and L.P. contributed to the scientific discussion of the results. Z.Z., A.Z. M.M. and Z.C. analyzed the experimental data and wrote the manuscript with the contributions of all other authors.

Competing interests

The authors declare no competing interests.

Additional information

Supplementary information The online version contains supplementary material available at <https://doi.org/10.1038/s41467-025-56113-4>.

Correspondence and requests for materials should be addressed to Alberto Zobelli, Marino Marsi or Zhesheng Chen.

Peer review information *Nature Communications* thanks the anonymous reviewers for their contribution to the peer review of this work. A peer review file is available.

Reprints and permissions information is available at <http://www.nature.com/reprints>

Publisher's note Springer Nature remains neutral with regard to jurisdictional claims in published maps and institutional affiliations.

Open Access This article is licensed under a Creative Commons Attribution-NonCommercial-NoDerivatives 4.0 International License, which permits any non-commercial use, sharing, distribution and reproduction in any medium or format, as long as you give appropriate credit to the original author(s) and the source, provide a link to the Creative Commons licence, and indicate if you modified the licensed material. You do not have permission under this licence to share adapted material derived from this article or parts of it. The images or other third party material in this article are included in the article's Creative Commons licence, unless indicated otherwise in a credit line to the material. If material is not included in the article's Creative Commons licence and your intended use is not permitted by statutory regulation or exceeds the permitted use, you will need to obtain permission directly from the copyright holder. To view a copy of this licence, visit <http://creativecommons.org/licenses/by-nc-nd/4.0/>.

© The Author(s) 2025